Data-driven Phase Synchronization of Harmony's Ocean Surface Topography Product

Andreas Theodosiou, *Student Member, IEEE*, and Paco López-Dekker, *Senior Member, IEEE*

***Abstract*—The Harmony mission features two bistatic synthetic-aperture radar (SAR) companions of Sentinel-1. As with any multistatic system, frequency deviations among the oscillators of the receivers cause a phase error in the phase of the demodulated SAR signal. Given that interferometry will be used to retrieve geophysical parameters from Harmony's radar instruments, an erroneous phase difference between the SAR signals of the two companions will bias the retrieval. The companions will use a global-navigation system (GNSS)-based method to synchronize the phase of the signals. The residual phase that remains after the synchronization is significant enough to make the retrieval of relative sea-surface height (RSSH) impossible. In this paper, we present Multisquint with Overlaps (MuSO), a data-driven algorithm to remove the synchronization residual. The algorithm uses the multisquint processing approach, together with the overlap regions of the TOPSAR acquisition mode, to estimate the derivative of the residual. After running the algorithm, simulations suggest that the error signal reduces from a standard deviation of 4° to 0.01°, allowing the retrieval of RSSH from Harmony data.**

***Index Terms*—SAR, interferometry, InSAR, formation flying, multistatic SAR, wide-swath ocean altimetry, phase synchronization, data-driven phase correction, GNSS phase synchronization, Harmony**

I. Introduction

BISTATIC and multistatic synthetic-aperture radars (SARs) offer the following advantages over monostatic SARs: flexible interferometric baselines, line of sight diversity, lower cost and simplicity of electronics due to a common transmitter. These benefits come at the cost of complexity, in terms of mission planning, operations, and processing. By definition, bistatic SARs use different oscillators to modulate the radar carrier at the transmitter and to demodulate the carrier at the receiver. Any deviation in the instantaneous frequency or phase of the oscillators introduces a phase error in the radar signal. The error will degrade any measurement that leverages the phase of the signal, such as synthetic-aperture radar interferometry (InSAR) and synthetic-aperture radar tomography-based measurements. Thus, in addition to the aforementioned costs, phase synchronization is an unavoidable challenge of multistatic systems.

The Harmony mission, which we introduce in more detail later in this section, consists of two bistatic SARs. The mission will use single-pass cross-track interferometry (XTI) for many of its measurements. Thus, phase synchronization is critical for Harmony, particularly for its experimental measurement of sea-surface height (SSH) because of the weak signal of interest relative to the phase error due to the asynchronous operation of the instruments. SSH is the elevation of the sea surface relative to the reference ellipsoid, and XTI measures the height variation relative to the mean height of the surface. In this paper, we refer to this relative elevation as relative sea-surface height. Using the height of the mean surface of an acquisition relative to the reference ellipsoid, one can obtain the SSH from measurements of the RSSH. Oceanographic studies, both theoretical and numerical, show that flows with horizontal scales in the order of $0.1\,\mathrm{km}$ to $10\,\mathrm{km}$, the so called *submesoscales* [1], play a critical role in the oceanic and atmospheric energy transfer, the mixing of heat and nutrients, and the sea state [1]–[4]. Measurements of the SSH at a resolution sufficient to resolve these scales are necessary to validate these studies and improve our understanding of oceanic physics.

Until recently, no remote sensing instrument was able to provide such measurements. The observational gap [5], was one of the primary motivations for the Surface Water and Ocean Topography (SWOT) mission of NASA/CNES [6]. SWOT characterizes ocean circulation from SSH measurements at spatial resolutions of $15\,\mathrm{km}$, by using a single-platform cross-track interferometer made of two Ka-band SARs.

Harmony, the European Space Agency's 10th Earth Explorer [7], consists of two satellites that will fly together with Sentinel-1. Each spacecraft will carry a passive SAR that will use Sentinel-1 as a transmitter, and a thermal infrared instrument. Harmony is a multipurpose mission that aims to quantify small-scale motion and deformation fields of the ocean surface, glaciers and ice sheets, and solid Earth [7]. In [8], the authors propose a measurement concept to retrieve RSSH using a formation of bistatic SARs, with the potential to resolve submesoscale RSSH. We have been working to introduce an experimental RSSH product for Harmony using this concept. However, the concept requires phase synchronization to work.

There are different techniques to synchronize bistatic SAR data. The most direct method, is using a bidirectional synchronization link between the satellites to exchange clock information, as employed in TanDEM-X [9], [10]. We refer to bistatic systems that exchange clock information as cooperative [11]. Cooperative systems require additional hardware to enable the information exchange between the satellites.

This work was supported in part by the European Space Agency (ESA) through the Harmony Phase-A Science Consolidation Studies under ESA Contract 4000134959/21/NL.

A. Theodosiou, is with the European Space Agency's European Space Research and Technology Centre, Postbus 299, 2200 AG Noordwijk, The Netherlands. P. López-Dekker is with the Department of Geoscience and Remote Sensing, Delft University of Technology, 2628 Delft, The Netherlands.

Phase synchronization of non-cooperative systems, i.e. systems that do not exchange clock information, unavoidably relies on information either directly from the SAR signals or from auxiliary data. Harmony is a non-cooperative system, as it does not have the means to exchange information between the companions. The impact of the lack of synchronization on bistatic SAR imaging was first discussed by Auterman in [12]. Massonet and Vadon discussed the use of repeat-pass interferometry to estimate the clock drift of the European Remote Sensing satellite [13]. The DLR-ONERA team discussed the synchronization of bistatic SAR signals, and demonstrated bistatic XTI from an airborne system [14]. The synchronization was based on information from monostatic and bistatic SAR signals. Estimating the synchronization phase from the received signals, also known as autosync, has been demonstrated with a spaceborne sensor using TanDEM-X experiments [15]. Autosync's performance depends on the backscattering of the scene, making it suboptimal for interferometric applications.

Recent advances in the field show that the phase synchronization error can be reliably corrected using a global navigation satellite system (GNSS) based technique [16]. This follows from the fact that the part of the GNSS solution is the phase difference between the GNSS-receiver reference clock and the GNSS reference. Therefore, after making sure that the GNSS-receiver and the radar payload share a common reference oscillator, phase-synchronization becomes a by-product of the Precise Orbit Determination (POD) step. The results of [16] suggest that this approach can estimate the phase synchronization error if systematic errors are suppressed. Specifically, at C-band the method achieves synchronization with a standard deviation of $1.6°$. Since the estimation of the error happens at the carrier frequency of the GNSS signal (L-band), the error of the solution scales, assuming spectral purity of frequency conversion stages, linearly with frequency, reaching a cutoff in terms of usability near X-band [16].

Harmony's RSSH error budget allocates a synchronization error with a $1.0\,\mathrm{cm}$ standard deviation [8]. This value is set to allow the resolution of RSSH at the submesoscales. By using the minimum and maximum interferometric sensitivity of Harmony reported in [17], we convert this value to a phase error of $0.04°$ to $0.10°$. Therefore, we need to improve upon the GNSS-based phase synchronization to make the retrieval of RSSH possible.

In this article, we present a data-driven correction algorithm that reduces the residual phase synchronization error that is left in the radar signal after the GNSS-based synchronization has been carried out. The algorithm suits the retrieval of small signals that require a high sensitivity, such as RSSH. Our algorithm builds upon Enhanced Multisquint Processing, introduced in [18], [19], as well as autosync [15], and uses the system inversion approach similarly to [20]. It leverages the overlap regions, where samples are acquired twice for the same region on the surface, of the Terrain Observation by Progressive Scans (TOPSAR) mode [21] by using the samples at the overlaps as additional more robust estimates of the finite difference of the phase synchronization residual.

The structure of the article is as follows: We start by introducing a model for the phase of the bistatic SAR signal due to the non-synchronous operation, and a model for the residual error that remains after GNSS-based synchronization in Section II. In Section V, we simulate the RSSH that Harmony would retrieve for a scene based on the outputs of a coupled ocean-atmosphere model in the Bay of Biscay, France, and run the algorithm on the simulated data. Section VI discusses the results and the performance of the algorithm in terms of the semivariogram, identifies three sources of errors, discuss potential solutions. Finally, in Section VII we conclude the article by giving an overview of potential improvements to the algorithm.

II. Origin and Characteristics of Phase Synchronization Error in Bistatic SAR

A. Where Does The Error Come From?

The separation of transmitter and receiver inherent in bistatic systems leads to the need for three different types of synchronization [22]:

1) Time or reception window synchronization: The reception window of the receiver must align or include the transmission window of the transmitter for the duration of the acquisition.
2) Beam synchronization: The transmit and receive antennas must illuminate the same region on the ground at the same time.
3) Phase synchronization: The difference in the instantaneous phases of the oscillators in the transmitter and the receiver must be minimized.

The algorithm of this article tackles 3). Bistatic SARs have spatially separate transmitter and receivers. Therefore, each receiver has its own oscillator with an independent instantaneous phase. The instantaneous phase of the ith receiver is [12], [23]

$$\psi_i(t) = 2\pi \int_{\tau_0}^{t} f_i(\tau)\,\mathrm{d}\tau + \phi_{i,0}, \tag{1}$$

where τ_0 is the initial time offset, $\{f_i(t), t \geq 0\}$ is a stochastic process representing the instantaneous frequency of the ith oscillator, and $\phi_{i,0}$ is a constant phase offset. f_i is the sum of the oscillator's central frequency, $f_{i,c}$, and a zero-mean stochastic process representing deviations from the central frequency, $\{\delta f_i(t), t \geq 0\}$ [16]

$$f_i(t) = f_{i,c} + \delta f_i(t). \tag{2}$$

Setting $i = u$ for the first receiver and $i = v$ for the second, we see that each oscillator will introduce a different instantaneous phase during the demodulation of the signals. When two SAR images from different receivers are interfered to form an interferogram, the phase of the first SAR signal is subtracted from that of the second. This operation leaves a phase synchronization error, $\psi_{vu}(t) = \psi_v(t) - \psi_u(t)$, present in the phase of the interferogram. The error remains even when the oscillators have the same central frequency as the deviations from the central frequency are independent processes.

B. Post-GNSS Synchronization Phase Residual

In [16] Rodrigues-Silva et al. present a GNSS-based synchronization scheme for multistatic SAR systems such as Harmony. By designing the system to share the oscillator between the satellite's GNSS receiver and the payload, the scheme estimates and corrects the phase synchronization from the combined navigation and precise-orbit determination data. The scheme achieves a residual error after correction with a standard deviation of 1.6° at C band. As discussed in II, such a standard deviation is insufficient for retrieval of RSSH.

Before correcting for it, one ought to first characterize the residual error signal after the GNSS synchronization. We model the signal as a stochastic process, $\{\psi_c(t), t \geq 0\}$ with a flat non-zero power spectral density (PSD) between $0\,\mathrm{Hz}$ and f_b, and a zero PSD outside this band

$$S_{\psi_c}(f) = \begin{cases} \dfrac{\sigma^2_{\psi_c}}{2f_b}, & \text{if } -f_b \leq f \leq f_b, \\ 0, & \text{otherwise.} \end{cases} \tag{3}$$

The non-zero part of the PSD has a value of $\sigma^2_{\psi_c}/(2f_b)$ and units of $\mathrm{rad}^2/\mathrm{Hz}$, where $\sigma^2_{\psi_c}$ is the variance of the residual phase post-GNSS correction. For the purposes of the simulations in this article, we set $f_b = 2\,\mathrm{Hz}$, $\sigma_{\psi_c} = 4^\circ$. We have arrived at the spectral characterization given by (3), and to the values of f_b and σ_{ψ_c} after consulting the authors of [16].

We simulate realizations of the residual error that adhere to (3) with the following procedure [24]:

1) Discretize the PSD.
2) Convert the discrete PSD to the amplitude of the Discrete Fourier Transform of ψ_c according to $\sqrt{N f_s S_{\psi_c}[f]}$, where N is the number of points in the discrete PSD, and f_s is the sampling frequency.
3) Assign a random phase to each point of the DFT of ψ_c for $f \geq 0$, sampled from a uniform distribution between 0 and 2π.
4) Set the phase of the negative frequencies of the DFT so that the DFT is even symmetric.
5) Compute the inverse DFT.

Figure 1a shows the PSD described by (3) and Figure 1b shows a realization of the stochastic process that has such a PSD. We have simulated the realization from the PSD according to the procedure we have described in the previous paragraph. In addition to the flat PSD of (3), we consider a Gaussian-shaped PSD with the $3\,\mathrm{dB}$ point at the cutoff frequency of the flat spectrum, and the same total power. The Gaussian-shaped PSD produces a phase synchronization residual with higher-frequency components than the flat PSD, allowing us to assess the performance of the algorithm when the signal to be estimated is changing more rapidly. We provide more information on the simulations with this alternative phase synchronization residual in the Appendix.

III. Correction Algorithm

A. Overview and Signal Model

The algorithm that we are presenting is designed to work on the interferometric phase residual after the GNSS-based synchronization of [16]. Consequently, the algorithm estimates a realization of the stochastic process described by (3) from noisy observations of its finite difference, i.e. approximations of the derivative obtained by the difference of the signal sampled at two different instants of time. We obtain the finite difference via two distinct methods: by computing the differential interferometric phase of the overlap regions, and by computing the differential interferometric phase of subaperture images. We introduce the terms "overlap regions", and "subapertures images" in the following two paragraphs.

The algorithm assumes the following: the SAR image has azimuth lines that are sampled twice at different instants of time, not more than a few seconds apart. From here on, we call these azimuth lines "overlap regions". The overlap regions occur periodically at fixed azimuth intervals, as is the case in TOPSAR mode [21]. In TOPSAR, the overlap regions occur whenever the instrument completes a scanning cycle and returns to a given subswath. To ensure that no gaps occur in azimuth between bursts, the first azimuth lines of a burst overlap with the last azimuth lines of the preceding burst. These overlap regions are typically not visible in processed SAR images because processors merge bursts by keeping the samples of only the early or the late burst for a given azimuth to create a continuous image.

The algorithm's second source of observations comes from subaperture images. SAR processing focuses the echoes that the instrument collects from each scatterer at different time instants, and consequently squint angles, during the illumination time to the correct resolution cell. The length of the synthetic aperture and the instrument's line of sight define the range of squint angles. The raw signal can be focused with a different central squint than that of the instrument, resulting in a SAR image with reduced bandwidth, known as a subaperture image. Several subaperture images can be formed out of a SAR image by focusing the raw signal with different central squints. Each subaperture image contains signal collected during the illumination time by a different part of the full aperture.

A fundamental assumption of the algorithm is that the geophysical signal remains constant during the illumination time, while instrument and platform induced errors vary continuously. Hence, by comparing the signal from different subaperture images, the instrument, and platform errors can be estimated. This technique is known as Multisquint Processing [25], and its variant of using more than two subapertures, Enhanced Multisquint Processing, has been used to correct for residual motion errors [18], estimate the azimuth motion of glaciers [19], and it has been proposed to synchronize the phase of tomographic acquisitions [20]. An additional assumption of the algorithm is that the geophysical signal remains constant during the cycle time of the TOPSAR acquisition. As we explain in the following paragraphs, a dynamic surface, such as the ocean, will have a time-varying contribution to the signal. In the rest of this subsection we introduce a preprocessing step that removes this component to enable the aforementioned assumptions to be met.

The heart of the algorithm lies in leveraging the variance and invariance of the synchronization residual and the topographic phase, respectively, between interferograms of adjacent sub-

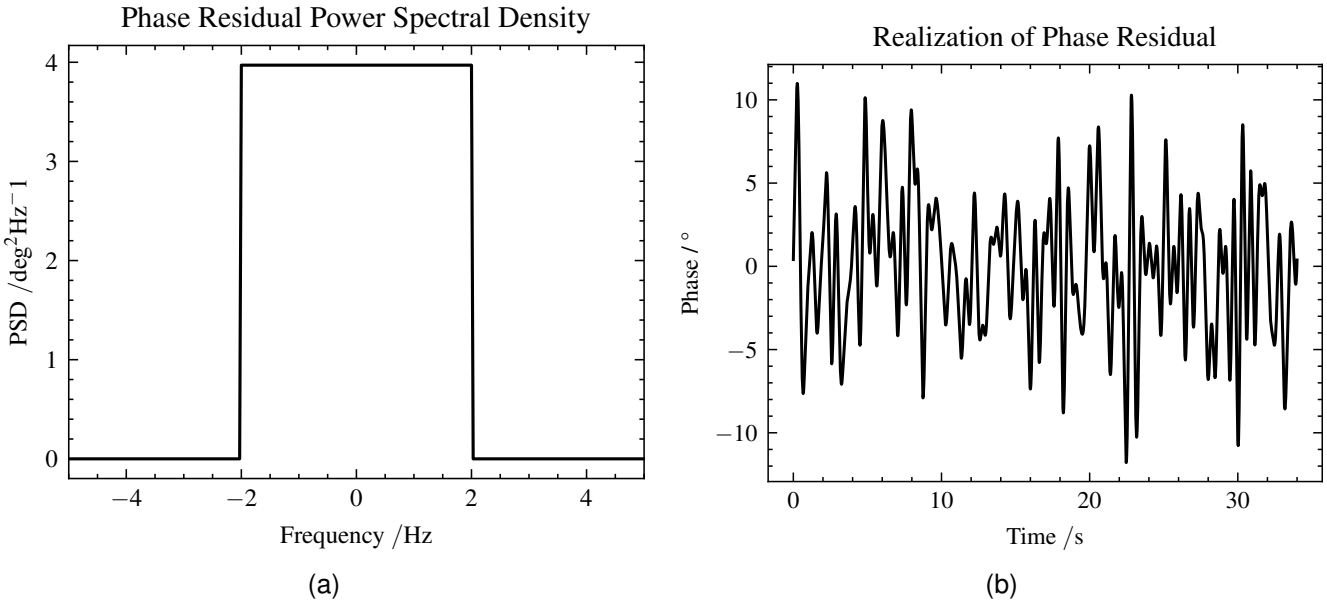

Fig. 1. The phase residual after applying the GNSS-based synchronization scheme is a stochastic process characterized by a flat narrowband spectrum. (a) The power spectral density. (b) A realization of the stochastic process.

apertures and overlap regions. We model the interferometric phase of the interferogram between the ith subapertures as

$$\phi_i(t,\tau) = \phi_t(t,\tau) + \phi_m(t_{c,i},\tau) + \psi_c(t_{c,i}) + n_i(t,\tau), \quad (4)$$

where t represents the slow time corresponding to an azimuth position in the focused image, $t_{c,i}$ represent the azimuth beam-center time of the ith subaperture, and τ is the range (fast) time. ϕ_i has several components, the topographic component ϕ_t, in the case that there is an along-track baseline between the SAR acquisitions a motion component ϕ_m, the synchronization residual ψ_c, and noise n_i.

We explicitly include the subaperture index i as subscript to highlight the assumption that the topographic phase stays constant in each subaperture, while the other phase contributions change with subaperture. Furthermore, we have assumed that the residual ψ_c does not vary with range because for a given azimuth position, samples are collected over the swath width in fractions of a millisecond, a time interval that is much shorter than the period of the highest frequency component of ψ_c.

The beam-center time of the ith subaperture is

$$t_{c,i} = t - \frac{T_a}{2} + \frac{T_a}{N}\left(i - \frac{1}{2}\right), \quad (5)$$

where T_a is the aperture time, and N is the number of subapertures [26]. Thus, the interferograms from different subapertures capture the phase synchronization residual at different time instants. Figure 2 serves as an example of the interferometric phase of the first subaperture for $N = 6$. Furthermore, the interferometric phase due to the motion of the surface also changes between the subapertures. The phase due to motion, also known as the along-track interferometric (ATI) phase is [27]

$$\phi_m = \frac{2\pi B_\parallel}{\lambda v_p} \boldsymbol{v_s} \cdot \hat{\boldsymbol{l}}_{\boldsymbol{i}} \quad (6)$$

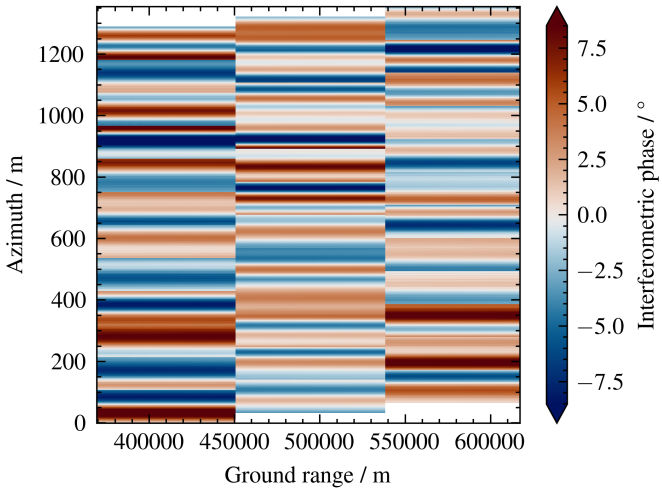

Fig. 2. Simulation of the subaperture interferometric noise. The noise in the phase has a variance that is N times higher, than the variance of the full aperture interferogram.

where $B_\parallel$ is the effective along-track baseline of the interferometer, v_p is the velocity of the platform, v_s is the vector representing the velocity of the surface, and $\hat{\boldsymbol{l}}$ is a unit vector parallel to the instrument's line of sight. Due to the relationship between time and frequency, each subaperture image contains the signal collected by the instrument with a different segment of the azimuth beamwidth [28]. Thus, each pair of subaperture images have a different central squint, and $\hat{\boldsymbol{l}}$ changes for each subaperture. The line of sight unit vector of the ith subaperture is

$$\hat{\boldsymbol{l}}_{\boldsymbol{i}} = \begin{pmatrix} \sin(\eta + \eta_i) \\ \cos(\eta + \eta_i)\sin\theta \end{pmatrix}, \quad (7)$$

where η is the squint of the line of sight, $\eta_i = -\frac{\beta}{2} + \frac{\beta}{N}(i - \frac{1}{2})$ is the squint offset with respect to η of ith subaperture, and β

is the instrument's azimuth beamwidth.

The phase of the differential interferogram between the interferogram of subaperture images i and that of subaperture images $i+1$, which we call the spectral diversity phase [18], is given by the following equation:

$$\Delta\phi_i(t,\tau) = \phi_m(t_{c,i+1},\tau) - \phi_m(t_c,\tau) + \psi_c(t_{c,i+1}) - \psi_c(t_{c,i}) + n_{i+1}(t,\tau) - n_i(t,\tau). \quad (8)$$

Equation (8) shows that the topographic phase cancels out in the differential interferogram. The phase due to motion, however, does not as it depends on the look direction which changes with subaperture. Thus, if the cross-track interferometer has an effective along-track baseline, which is unavoidable in formation-flying systems, the spectral diversity phase will have a motion component, a residual synchronization component, and noise.

The motion component of the spectral diversity phase is [29]

$$\Delta\phi_{m,i}(t,\tau) = \frac{2\pi B_\parallel}{\lambda v_p} 2\sin\frac{\beta}{N}\big(-2s_\rho\sin(\eta+m_i) + 2s_a\cos(\eta+m_i)\big), \quad (9)$$

$$= \frac{2\pi B_\parallel}{\lambda v_p} 2\sin\left(\frac{\beta}{N}\right)\boldsymbol{v_s}\cdot\hat{\boldsymbol{x}}_{\boldsymbol{i}}, \quad (10)$$

where $m_i = \beta(-1/2 + i/N)$, $\eta + m_i$ is the mean squint of the subapertures used to form the spectral diversity phase, and $\hat{\boldsymbol{x}}_{\boldsymbol{i}} = (\cos(\eta+m_i), -\sin(\eta+m_i))^T$ is the azimuth direction defined by m_i. We have identified the term inside the brackets in (9) as the projection of the velocity vector on the mean azimuth direction of the subapertures that form the differential interferogram. Therefore, the spectral diversity phase of adjacent subapertures is directly proportional to the motion in the mean azimuth direction. Importantly, for N subapertures, one can form $N-1$ spectral diversity phases and each will have an azimuth motion component. The mean azimuth direction rotates in increments of $\frac{\beta}{N}$ between successive subaperture pairs.

Spectral diversity techniques, including multisquint processing, assume that no geophysical signal is present in the spectral diversity phase. Thus, they treat the spectral diversity phase as an estimate of the derivative of azimuth errors. The integral of the spectral diversity phase yields an estimate of the azimuth error, which they use to correct the interferograms. The assumption is valid in scenes where the surface is static in the time between the SAR acquisitions, which is the case over land. From (10), we can tell that this assumption is invalid for dynamic surfaces, such as the ocean.

Consequently, we need to remove the azimuth motion component from the spectral diversity phase before using it to estimate the phase synchronization residual. The Harmony satellites feature an antenna that has a fore, and an aft phase center. Each satellite forms two SAR images from the signals received by the fore and aft phase centers. We will refer to these as the individual phase center (IPC) images. They then combine the signals received by these phase to form an improved SAR image, that we will call the combined phase center (CPC) image.

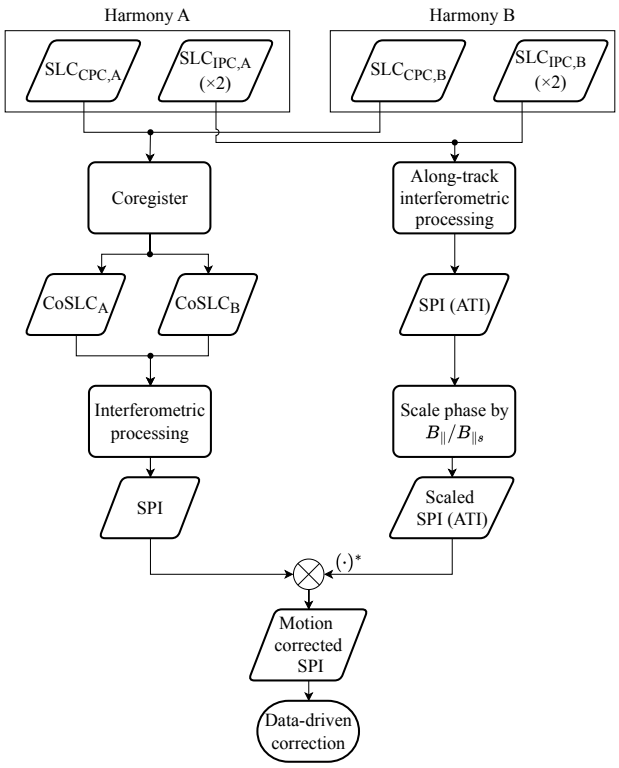

Fig. 3. High-level flowchart of the Harmony single-pass interferogram generation, including the removal of the ATI phase. $\mathrm{SLC_{CPC,i}}$ stands for the SLC image of the combined phase center, and $\mathrm{SLC_{IPC,i}}$ represents the SLC image of the individual phase centers coming from the wing antennas of each Harmony companion, where subscript i can be A or B to refer to the first or second companion respectively. $\mathrm{CoSLC_i}$ refers to the coregistered SLC image, SPI is the single-pass interferogram, $B_\parallel$ is the interferometric along-track baseline of the satellite formation, and $B_{\parallel s}$ is the along-track baseline of the fore and aft phase centers. In the diagram, the $\times 2$ annotation next to the $\mathrm{SLC_{IPC,i}}$ highlights that each companion produces two SLC images from the two wing phase centers, and the along-track interferometric processing involves the creation of an interferogram from two independent pairs of SLC images.

The phase centers are separated along the azimuth direction of the antenna, thus having an effective along-track baseline. Therefore, we can perform along-track interferometry with the SAR images from the individual phase centers to estimate the ATI phase. By scaling the estimate by the ratio of the effective along-track baseline of the formation to the along-track baseline of the on-board phase centers, we can compute the ATI phase of the CPC interferogram. Once we have an estimate of ϕ_m we can subtract it from the phase of the interferogram [8]. Then, the subaperture-dependent motion component will be eliminated from the spectral diversity phase and (8) will only include the synchronization residual term and noise. Figure 3 shows a flowchart of the interferogram generation, including the correction of the ATI phase.

The ATI phase estimate from the IPCs will have an error with respect to the true ATI phase that is determined by the coherence of the IPC SAR images. Scaling the ATI phase and subtracting it from the interferometric phase of the CPCs will increase the noise of the interferometric phase. Therefore,

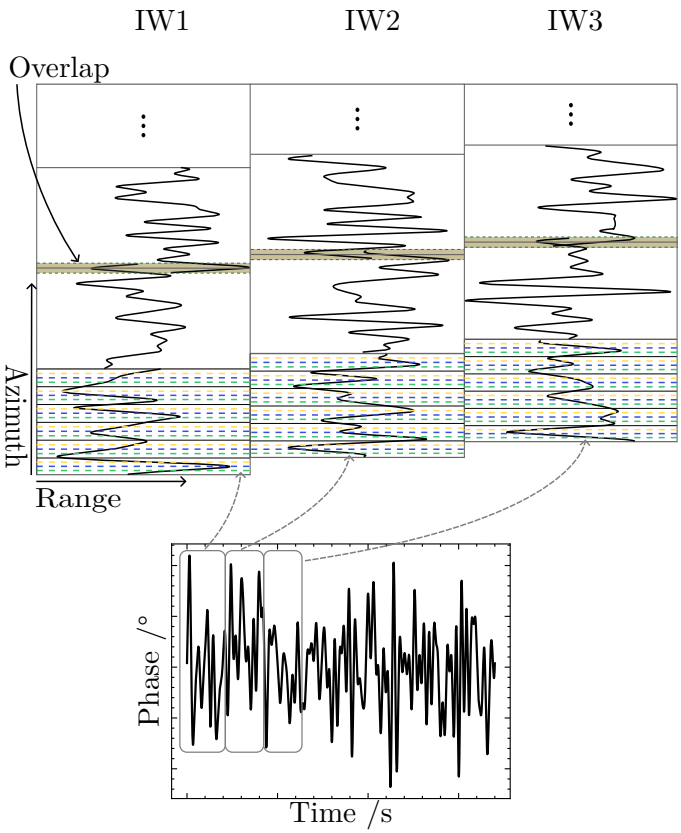

Fig. 4. Schematic showing how the phase residual of Figure 1b, shown in the bottom panel, maps into the bursts, and subswaths of an Interferometric Wide Swath (IW) interferogram, shown in the top panel. In the top panel, the horizontal gray lines represent the burst boundaries, while the black lines within the first burst of each subswath represent the boundaries of azimuth resolution cells. The dashed blue, green, and yellow line represent the sampling time of the full aperture, a subaperture with a forward squint, and a subaperture with a backward squint respectively. The shaded areas within the dashed green lines represent the overlap regions. The overlap regions, and the subapertures occur in every burst, however they are not shown together in the figure for clarity. The figures, including the number of resolution cells, and the length of the bursts and of the overlap regions are illustrative and not to scale.

removing the bias due to surface motion comes at the cost of making the interferometric, and by extension the spectral diversity, phase noisier.

B. Derivative Estimation using Adapted Enhanced Multisquint Processing

Once the subaperture interferograms have been cleaned from the phase due to motion, the spectral diversity phase becomes

$$\Delta\phi_i(t,\tau) = \psi_c(t_{c,i+1}) - \psi_c(t_{c,i}) + n_{\mathrm{sd},i}(t,\tau), \tag{11}$$

where $n_{\mathrm{sd},i}$ represents the noise of the spectral diversity phase. $n_{\mathrm{sd},i}$ includes the error from the subaperture interferogram and the error of the ATI phase correction. Hence, we can now treat the spectral diversity phase as the finite difference of the synchronization residual and apply an adaptation of Enhanced Multisquint Processing [18]. Figure 4 illustrates the mapping of the synchronization residual to the bursts, and subswaths of an IW interferogram. In the first three bursts of each subswath, the dashed lines show the sampling times of the full aperture, and two subapertures. The spectral diversity phase corresponds to the difference between the samples occurring at the green dashed line, and the samples occurring at the yellow dashed line.

Following Enhanced Multisquint Processing we use multiple subapertures to compute the differential interferometric phase. The number of subapertures is a parameter of the algorithm. The temporal separation between subaperture interferometric phases decreases as the number of subapertures increases according to $\Delta t = T_a/N$. Thus, increasing the number of subapertures allows the algorithm to track rapidly varying parts of the signal. At the same time, more subapertures means that each subaperture uses less azimuth bandwidth, resulting in more noisy subaperture interferograms.

Using multiple subapertures and then combining them combines the benefit of short aperture times while maximizing the use of the available bandwidth. Thus, we produce N subapertures, from which we create $N-1$ spectral diversity phases. Each spectral diversity phase samples the finite difference of the interferogram phases at

$$t_{\mathrm{sd},i} = t_{c,i} + \frac{T_a}{2N}. \tag{12}$$

As a result, to average the spectral diversity phases we first need to resample them to the sampling times of the full aperture interferogram. The averaged spectral diversity phase is

$$\Delta\phi(t) = \frac{1}{N-1}\sum_{i=1}^{N-1}\sum_{k=0}^{M-1} \mathrm{sinc}\left(\frac{t - t_{\mathrm{sd},i}[0] - kT}{T}\right)\Delta\phi_i[k], \tag{13}$$

where $\Delta\phi_i[k]$ represents the kth sample of the ith spectral diversity phase. The square brackets denote a discrete-time signal $\Delta\phi_i[t] \coloneqq \Delta\phi_i(t_{sd,i}[0] + kT)$ with $T = 1/f_s$ where T is the sampling period and f_s the sampling frequency. Using the same notation, $t_{\mathrm{sd},i,}[0]$ is the initial value of the ith spectral diversity slow time. Finally, M is the number of samples per subaperture.

Taking the mean value of the average spectral diversity phase over range, and dividing by the temporal separation of adjacent subapertures, Δt, yields an estimate of the derivative of the synchronization residual at t,

$$\hat{\psi_c}'(t) = \frac{\mathbb{E}_\tau\left\{\Delta\phi(t,\tau)\right\}}{\Delta t}, \tag{14}$$

where $\mathbb{E}_\tau$ is the expectation operator over range.

C. Overlap Regions

In addition to the estimate of the derivative, the algorithm leverages the differential interferogram between two full-aperture interferograms at the overlap regions to measure the finite difference of the synchronization residual, $\Delta\psi_c$, at the azimuths that fall within these regions. The measurements from the overlap regions use the full bandwidth of the signal. Thus, these measurements are expected to be more accurate than the multisquint-based derivatives. Finally, since the time

difference between the samples of the overlap regions is larger than the difference between adjacent subapertures, the overlap difference can correct for slow drifts in the estimated solution that a purely multisquint-based solution might miss.

As the shaded areas of Figure 4 show, the overlap regions occur at the beginning of each burst, and last a fraction of the burst. The overlap regions are a product of the cyclic scanning of the instrument in TOPSAR. After the completion of a cycle, the instrument begins a new burst by illuminating a given subswath with the first azimuth lines being the same as the last azimuth lines of the preceding burst. Given that the overlap regions are a fraction of the burst length, they can only provide a periodic correction to the phase error at the beginning of each burst. Nevertheless, since the phase finite difference from the overlaps comes from the full-aperture SAR images, and not from subapertures, the finite differences have less noise than the differential phase of the subaperture interferograms. Specifically, the coherently averaged spectral diversity phase has noise with variance $N/(N-1)$ times higher than the finite difference of the overlap regions.

D. MuSO: Joint Multisquint and Overlap Region Inversion

Combining the multisquint-based derivatives with the overlap differences allows us to design an estimator that uses more information than using a purely mulstisquint-based approach. To sum up, we have the following two sets of observations:

1) The multisquint-based derivative of the synchronization residual at each instant of sensing time.
2) The difference of the synchronization residual at the overlap regions from the full-bandwidth differential interferogram.

To estimate the synchronization residual from these observations we formulate the problem as a linear system

$$\begin{pmatrix} \hat{\psi_c}'[0] \\ \hat{\psi_c}'[1] \\ \vdots \\ \hat{\psi_c}'[N-2] \\ \Delta\psi_{co}[0] \\ \vdots \\ \Delta\psi_{co}[K-1] \\ 0 \end{pmatrix} = \begin{pmatrix} \boldsymbol{\Delta} \\ \boldsymbol{O} \\ \boldsymbol{J_{1,N}}/N \end{pmatrix} \begin{pmatrix} \psi_c[0] \\ \psi_c[1] \\ \vdots \\ \psi_c[N-1] \end{pmatrix}. \quad (15)$$

$\psi_c[n]$ represents the nth sample of the synchronization residual and the square brackets denote a discrete-time signal $\psi_c[n] \coloneqq \psi_c(nT)$ with $T = 1/f_s$ where T is the sampling period and f_s the sampling frequency. $\Delta\psi_{co}[n]$ is the nth sample of the signal's finite difference at the overlap regions. $\boldsymbol{\Delta}$ is an $(N-1) \times N$ matrix, $\boldsymbol{O}$ is a $K \times N$ matrix, and $\boldsymbol{J_{1,N}}$ is the $1 \times N$ unit matrix. Together they form the system's design matrix. The three matrices are defined as follows:

$$\boldsymbol{\Delta} = \operatorname{diag}(\boldsymbol{\Delta t}) \begin{pmatrix} 1 & -1 & 0 & \dots & 0 \\ 0 & 1 & -1 & \dots & 0 \\ 0 & 0 & 1 & \dots & 0 \\ \vdots & \vdots & \ddots & \ddots & \vdots \\ 0 & 0 & \cdots & 1 & -1 \end{pmatrix} \quad (16)$$

$$\boldsymbol{O}_{i,j} = \begin{cases} 1, & \text{if } j \text{ is the early sample of the } i\text{th overlap,} \\ -1, & \text{if } j \text{ is the late sample of the } i\text{th overlap,} \\ 0, & \text{otherwise,} \end{cases} \quad (17)$$

$$\boldsymbol{J_{1,N_k}} = 1 \quad (18)$$

for $k = 1, 2, \dots, N$. We use $\boldsymbol{J_{1,N}}$ to provide an additional equation to the system, postulating that the mean value of the residual is 0°. The vector $\boldsymbol{\Delta t}$ of length $N-1$ represents the temporal separation between subapertures. Since each subswath has a different aperture time, the vector takes values $1/\Delta t_1$, $1/\Delta t_2$, and $1/\Delta t_3$ for the subaperture separation of the first, second, third subswath respectively,

$$\boldsymbol{\Delta t}_i = \begin{cases} \dfrac{1}{\Delta t_1}, & \text{if the } i\text{th sample comes from subswath 1,} \\ \dfrac{1}{\Delta t_2}, & \text{if the } i\text{th sample comes from subswath 2,} \\ \dfrac{1}{\Delta t_3}, & \text{if the } i\text{th sample comes from subswath 3.} \end{cases} \quad (19)$$

Equation (15) describes an overdetermined system of equations with N parameters and $N+K$ observations. We estimate the parameters by inverting the system using weighted least squares (WLS) and setting the weights to the inverse of the variance of the observations. We define the weight matrix as follows:

$$\boldsymbol{W} = \operatorname{diag}\big(\sigma_{sd}[0]^{-2}, \dots, \sigma_{sd}[N-2]^{-2}, \sigma_0[0]^{-2}, \dots, \sigma_0[K-1]^{-2}, (100 \max \sigma_{sd})^{-2}\big), \quad (20)$$

where the standard deviation of the spectral diversity derivative of the phase, ψ_c', relates to the standard deviation of the subaperture phase, according to

$$\sigma_{sd}[i] = \frac{\sqrt{2}}{\sqrt{N-1}\boldsymbol{\Delta t}_i} \sigma_{\text{sub}}[i]. \quad (21)$$

σ_{sub} is the standard deviation of the subaperture phase. We use the Cramer-Rao lower bound (CRLB) of interferometric phase and the ratio of the subaperture bandwidth, B_{sub}, to the full-aperture bandwidth, B_a, to define σ_{sub} [30]

$$\sigma_{\text{sub}} = \sqrt{\frac{1-\gamma^2}{2N_L\gamma^2} \frac{B_a}{B_{\text{sub}}}}, \quad (22)$$

where γ is the interferometric coherence, and N_L is the number of looks. The standard deviation of the differential phase at the overlap regions is given by

$$\sigma_0[i] = \sqrt{\sigma_{\psi_c}[l_i]^2 + \sigma_{\psi_c}[k_i]^2}, \quad (23)$$

where l_i is the late sample of the ith overlap, and k_i is the early sample of the ith overlap. We set the weight of the prior to correspond to a variance that is larger than the maximum variance of the observations. This is because we want the algorithm to give more weight to the observations than the prior assumption.

TABLE I
PARAMETERS USED IN THE SIMULATION EXPERIMENTS.

Parameter	Value	Unit
Center frequency	5.405	GHz
Mean platform ground speed	7161	$\mathrm{m\,s^{-1}}$
Incident angle Senintel-1 (IW)	30–46	$^\circ$
Mean lag between S1 and Harmony formation	350	km
Focused burst duration	3.0	s
TOPSAR cycle time	2.75	s
Number of bursts within acquisition	8	-
Number of subapertures	6	-
Total power of ψ_c	16	deg^2
Duration of sync residual to be estimated	33.0	s
Interferogram resolution used for data-driven sync	200×200	m^2
Mean height of ambiguity at near range	38.2	m
Mean height of ambiguity at far range	67.4	m

IV. Estimator Evaluation Metrics

In the subsequent sections, we will present and discuss the performance of the algorithm in terms of two metrics, the root mean squared error (RMSE), and the semivariogram. To help the reader in following the discussion, we define these metrics in this section.

After inversion of (15) using WLS, we obtain an estimate of the synchronization residual, $\hat{\psi}_c$. The RMSE of the estimator is

$$\mathrm{RMSE}(\hat{\psi}_c) = \sqrt{\mathbb{E}((\hat{\psi}_c - \psi_c)^2)}. \tag{24}$$

The RMSE provides a single value to assess the performance of the estimator.

The second metric that we use, the semivariogram is a function, describing the spatial dependence of a random field. It measures the variance of the difference between values the random field at different locations across realizations of the field. Mathematically, we can define it as [31], [32]

$$\gamma_\psi(\boldsymbol{x_1}, \boldsymbol{x_2}) = \frac{1}{2}\,\mathrm{var}(\Psi(\boldsymbol{x_1}) - \Psi(\boldsymbol{x_2})), \tag{25}$$

where Ψ represent the random field, and $\boldsymbol{x_1}, \boldsymbol{x_2}$ are the position vectors at which the field is evaluated. For wide-sense stationary processes, the semivariogram reduces to the expectation of the squared difference between values of a random field at different locations, where it is a function of only the distance between locations. Since we do not know the random field, we estimate the experimental, or empirical, semivariogram from the data using the Matheron estimator [33].

V. Simulations and Results

A. Simulations

In order to assess the performance of the algorithm, we simulate the multilooked interferometric phase that Harmony in its XTI phase would produce. Table I lists the relevant parameters of the simulations. We break down the simulation into three components:

1) We use coupled ocean-atmosphere models to model an oceanic scene. The variables of interest include RSSH, surface current vector, wind vector, and two-directional wave spectrum.
2) We pass the outputs of the ocean-atmosphere model to Harmony's scientific workbench, the mission's simulator for heterogeneous ocean scenes, and run the simulator to produce the multilooked normalized radar cross-section (NRCS) of the scene.
3) We feed the scene observables and the NRCS into Harmony's XTI performance model [8] to estimate the height of ambiguity and the standard deviation of the interferometric phase.

Once we have the results from these three operations, we can construct synthetic images of the multilooked interferometric phase. We do so by constructing the TOPSAR sensing timeline, i.e. the chronological sequence by which the instrument samples the surface including the order in which it switches between subswaths, and bursts. We break the interferogram into bursts and assign a sensing time to each azimuth line within each burst. We simulate the burst overlaps by repeating the last azimuth lines of the current burst at the first azimuth lines of the next burst for each subswath. The repeated azimuth lines of the overlaps have non-overlapping sensing times that are separated by the cycle time of the TOPSAR mode.

We assign a phase to each resolution cell of the interferogram by taking the height from the RSSH of the model, converting it to a phase using the height of ambiguity of the cell, and adding noise to it according to the CRLB. Additionally, we generate a realization of the synchronization residual as described in Section II-B and then resample it to the sensing times of the interferogram cells. Since each azimuth line of each subswath, including the lines of the overlapping regions, has its own sensing time, a different phase synchronization residual is assigned to each cell even if they are spatially overlapping.

Once we have the interferometric phase and the phase synchronization residual of each cell, we proceed with simulating the subapertures. For each azimuth line, we interpolate the synchronization residual to N different times according to (5). We then add noise, which we model as a zero-mean Gaussian with a standard deviation given by (22), to each of the subaperture phases. Next, we form $N-1$ spectral diversity phases by subtracting adjacent subapertures from one another as per (11), and then we coherently average them as described in (13).

With the averaged spectral diversity phase computed, we proceed with converting the spectral diversity phases into derivatives by dividing each sample by Δt_i, and averaging in range. Furthermore, we compute the overlap differential phases by finding the difference in interferometric phase at the overlap regions. Finally, we form the linear system of (15), define $\boldsymbol{W}$ using the standard deviation of each cell computed by the performance model, and solve for ψ_c.

B. Results

We simulate an interferometric acquisition of Harmony over the ocean and in particular over the coast of France. We use numerical model data from the MARC project [34]–[36] which uses Ifremer's MARS 2D [37], 3D [38] models, and

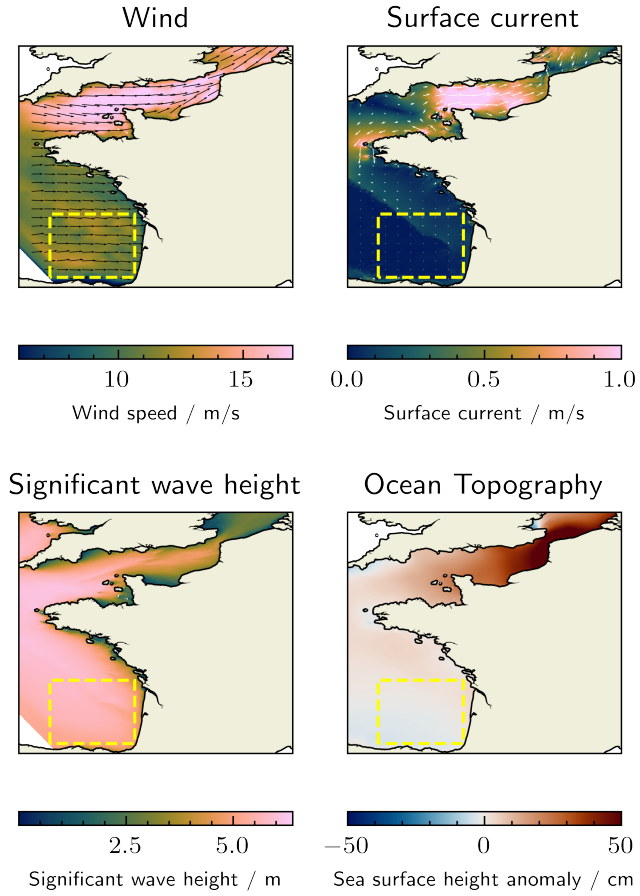

Fig. 5. Outputs from ocean-atmosphere coupled model. Clockwise from top left: Stress-equivalent wind; Surface current; Significant wave height; Sea-surface height anomaly. The area used for the simulated Harmony acquisition is indicated by the dashed yellow rectangle.

the WAVEWATCH III model [39]. After taking the wind, current, and wave spectra from the data, we resample them to a common $1\,\mathrm{km} \times 1\,\mathrm{km}$ grid, and cut a $250\,\mathrm{km} \times 255\,\mathrm{km}$ slice in range and azimuth, respectively, to use as the acquisition. Figure 5 shows the wind, current, significant wave height, and sea-surface height anomaly predicted by the MARC project on 2024-01-01 at midnight, while Figure 6 illustrates the directional wave spectrum from WAVEWATCH III.

The region that is used to simulate a Harmony acquisition is enclosed within a yellow dashed rectangle. The area shows medium wind and weak current, which will produce a medium signal-to-noise ratio. We note to the reader that the model provides the sea-surface height anomaly, i.e. the height relative to the temporal mean of the sea-surface height at a given location. In our simulations, we use this model output as the RSSH. The two quantities have similar dynamic range over the same spatial scales; thus, the anomaly serves as a realistic simulation of the RSSH. The height anomaly in the region is weak, varying between $-4\,\mathrm{cm}$ to $4\,\mathrm{cm}$. Thus, the scene will be a stress test for both the correction algorithm and the performance of the instrument (expected accuracy in medium wind of approximately $5\,\mathrm{cm}$).

Collecting the data that Figures 5 and 6 illustrate corresponds to step 1 of the preprocessing components outlined in section V-A. After completing the remaining steps, we form full- and subaperture images of the interferometric phase and run the algorithm on them. We also run a simplified version of the algorithm that does not use the overlap regions. This simplification corresponds to dropping the samples $\Delta\psi_{co}[0], \ldots, \Delta\psi_{co}[K-1]$ from the observations vector on the left-hand side of (15), and $\boldsymbol{O}$ from the right-hand side of (15).

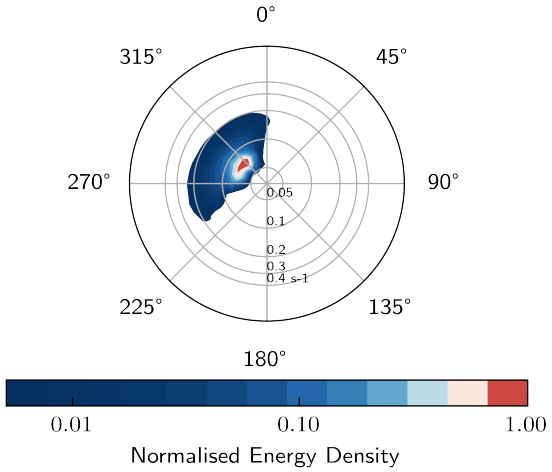

Fig. 6. Directional wave spectrum from WAVEWATCH III model.

The top panel of Figure 7 shows the true RSSH within the acquisition. The field corresponds to the yellow rectangle in the bottom right panel of Figure 5. The bottom panel of Figure 7 shows the height that Harmony would retrieve without correction, and with taking the measurement noise into account. The measurement noise has an average standard deviation in the ground range direction of approximately $6\,\mathrm{cm}$ to $8\,\mathrm{cm}$ at a resolution of $1\,\mathrm{km} \times 1\,\mathrm{km}$. There are gaps at the top and bottom of the three subswaths due to the TOPSAR operation.

Figure 8 illustrates the retrieved height after running the correction algorithm. The top panel shows the result after correcting without taking advantage of the information at the overlap regions, while the bottom panel shows the result after correcting with the information at the overlap regions. We illustrate the error between the synchronization residual estimated with the overlaps and the true synchronization residual in Figure 9. Figure 10 shows the same error but in terms of height.

The error between the true and estimated signal provides a metric on the performance of the algorithm. However, it lacks information on the spatial dependence of the algorithm performance. We use the semivariogram [32] to assess the spatial dependence of uncorrected and corrected signals. We compute the directional semivariograms of the uncorrected noisy RSSH, i.e. the signal shown in the bottom panel of Figure 7. Figure 11 shows the semivariogram in the range direction, and Figure 12 shows the semivariogram in the azimuth direction. The top panels of the figures show the histograms of the lag classes used for the experimental semivariograms and the green lines

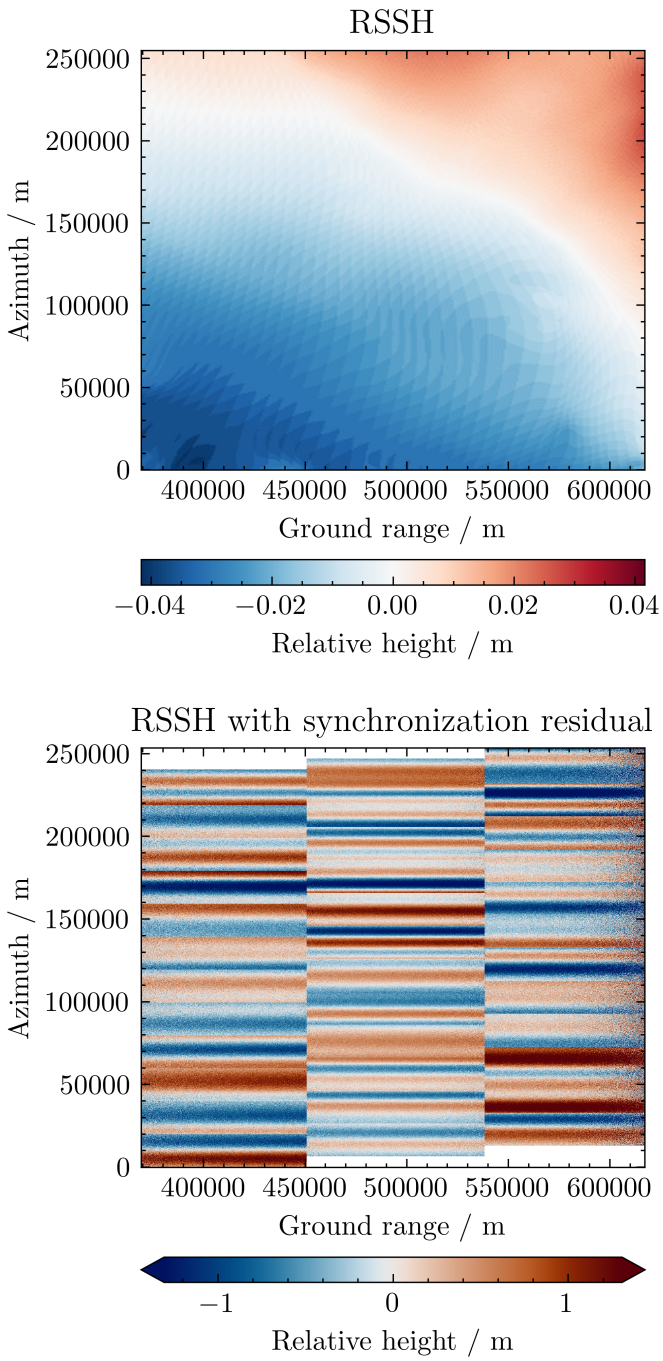

Fig. 7. Top: RSSH from the MARS-3D model. Bottom: Retrieved RSSH by Harmony without correcting for the phase synchronization residual.

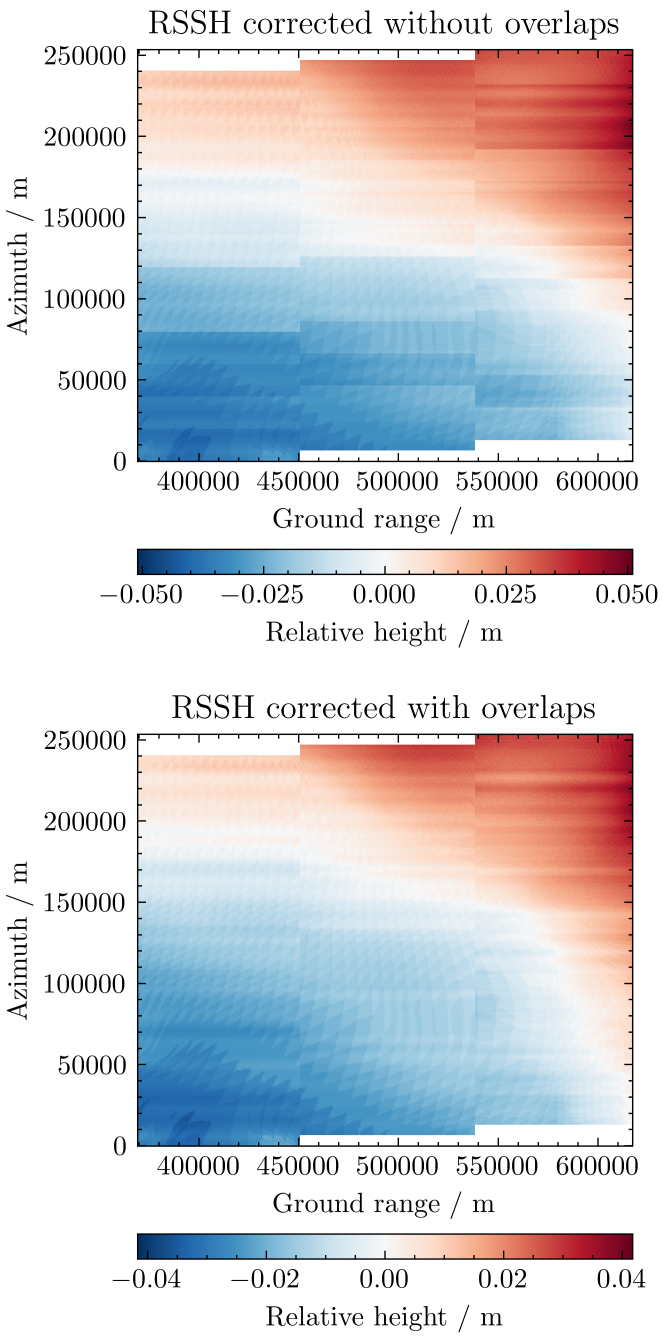

Fig. 8. Top: Corrected retrieved RSSH without using the information in the overlap regions. Bottom: Corrected retrieved RSSH with the information in the overlap regions.

in the bottom panels show a Gaussian model fitted to the data.

Figure 13 illustrates a more realistic result. The figure presents the retrieved corrected height with measurement noise. The measurement has been processed with a Gaussian filter to a resolution of $5\,\mathrm{km} \times 5\,\mathrm{km}$. Figures 14 and 15 illustrate the directional semivariograms of the corrected RSSH, prior to filtering, in the range and azimuth directions, respectively. We have set the maximum lag to not exceed half the extent of the scene [31], in the computation of the semivariograms.

VI. Discussion

A. Overview

We analyze in this section the results, and identify the strengths and weakness of the proposed data-driven correction method. In section VI-B we identify certain patterns in the corrected data and discuss their origins. Furthermore, we assess the performance of the data-driven correction in terms of estimation error, RMSE, and the semivariogram. Finally, in section VI-C we discuss the effect of the scatterer azimuth motion, and the subaperture duration on the correction.

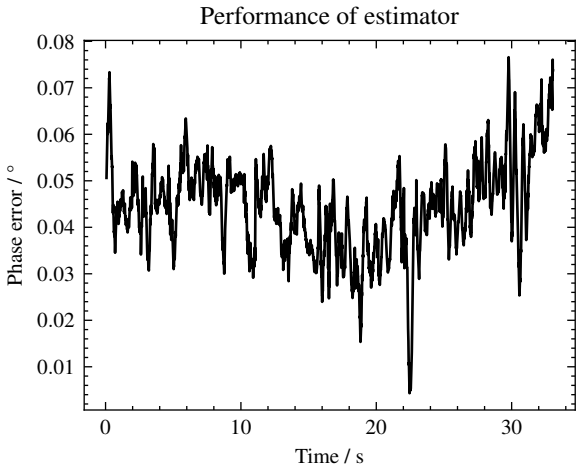

Fig. 9. Estimate error between the true phase synchronization residual and the estimated synchronization residual. The error centers about $0.044°$ because of the lack of knowledge of the integration constant during the estimation.

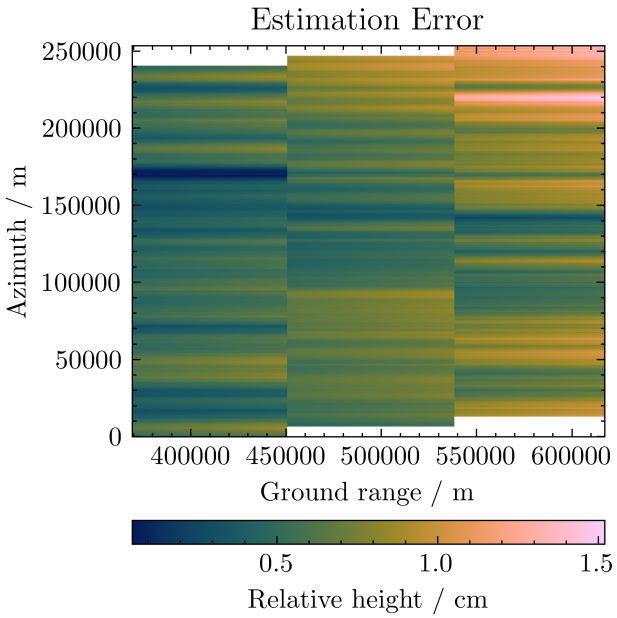

Fig. 10. Estimate error between the true phase synchronization residual and the estimated synchronization residual in terms of relative height. The error is the difference between the top panel of Figure 7, with the offsets in azimuth due to TOPSAR accounted for, and the bottom panel of Figure 8.

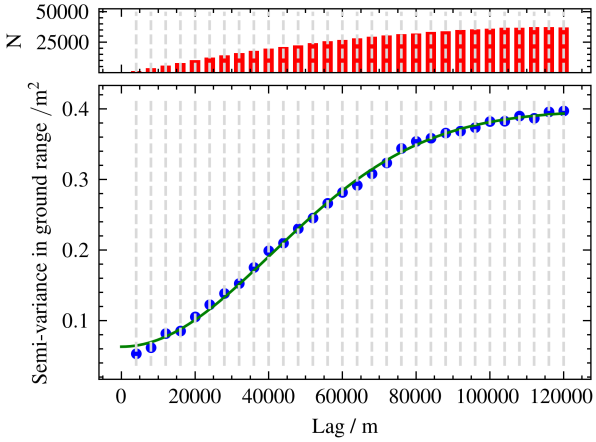

Fig. 11. The directional semivariogram of the uncorrected retrieved RSSH, shown in the bottom panel of Figure 7, in the ground range direction. The effective range is $117\,\mathrm{km}$ and binning of the samples used to compute the semivariogram are shown at the top panel.

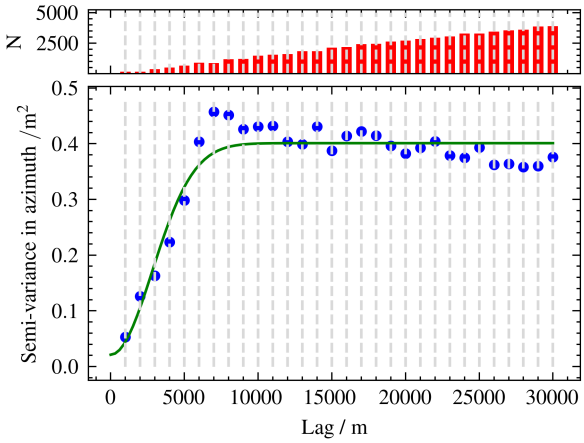

Fig. 12. The directional semivariogram of the uncorrected retrieved RSSH, shown in the bottom panel of Figure 7, in the azimuth direction. The effective range is $7.5\,\mathrm{km}$ and binning of the samples used to compute the semivariogram are shown at the top panel.

B. Performance of Data-driven Correction

The top panel of Figure 7 introduces the RSSH of the scene. The signal varies from $-4\,\mathrm{cm}$ in the southwest corner of the scene to $4\,\mathrm{cm}$ in the northeast. A prominent front features along the northwest to southeast axis where the height anomaly goes through $0\,\mathrm{m}$.

The bottom panel demonstrates the core issue. The post-GNSS phase synchronization residual overshadows the signal, obscuring the RSSH of the scene. Measurement noise is evident in the figure, especially at the edges of the sub-swaths where the NESZ declines. However, this noise is less prominent than the horizontal stripe pattern caused by the phase synchronization residual. This illustrates our previous assertion that without an additional correction, the phase synchronization residual will dominate the error budget.

The retrieved heights shown in Figure 8 demonstrate that the proposed algorithm successfully estimates and removes most of the phase synchronization residual. The top panel illustrates that correcting the signal without using the overlaps removes the majority of the synchronization residual. Artifacts are visible particularly near burst boundaries. The lack of sampling of the residual difference between TOPSAR cycles likely causes these artifacts. Taking advantage of the differential phase at the burst overlaps enhances the correction and removes the block-shaped artifacts, as shown in the bottom panel of Figure 8.

The observant reader will notice that the corrected signal is more positive than the true RSSH. This is noticeable particularly at the southeast corner, where the corrected signal has a lighter blue color in Figure 8 than in the top panel of Figure 7. The shift is due to the unknown integration constant that cannot be estimated from the derivatives of the signal. The last line of (15) essentially postulates that the integration

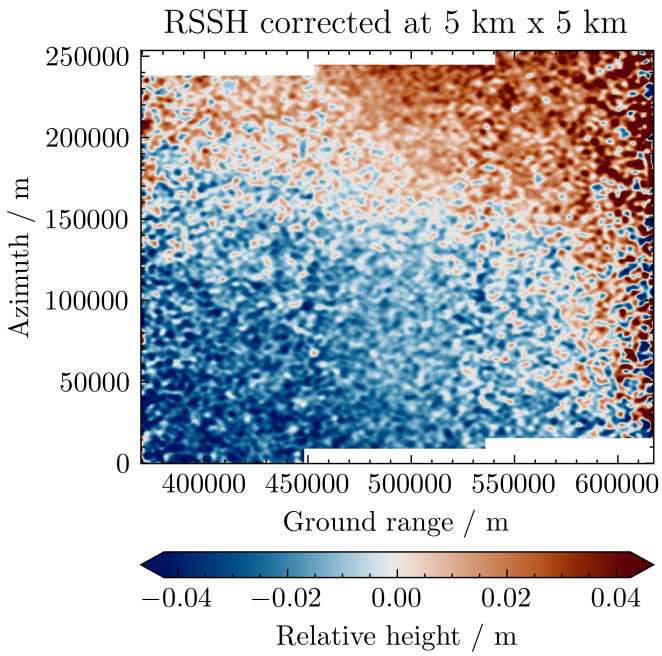

Fig. 13. Corrected retrieved RSSH, with measurement noise filtered at $5\,\mathrm{km} \times 5\,\mathrm{km}$.

constant equals zero, yet this not true. This prior assumption causes the estimator to under- or overestimate the synchronization residual at all times. In cases where the synchronization residual has a positive average value, i.e. when the signal is centered on a positive value, the estimator will underestimate the signal, while when the residual has a negative average value, the estimator will overestimate it as it will always push the estimate towards $0°$. Figure 9 demonstrates this shift. The error fluctuates about $0.044°$ which is the mean value of the synchronization residual.

Despite the shift, the estimator follows the true signal and provides an estimate that tracks the high- and low-frequency variations of the synchronization residual. Given that a cross-track interferometer estimates the relative height of the surface, a constant shift becomes a bias that does not affect the relative height error. The correction accuracy in terms of the RMSE is $0.046°$ when the algorithm with the overlaps is used, and it deteriorates to $0.062°$ when the overlaps are neglected. The constant shift dominates the RMSE. To assess the ability of the correction to capture the fluctuations of the synchronization residual, we compute the RMSE after removing the mean of the residual from it. Then, the RMSE drops to $0.010°$ and $0.043°$ for the correction with the overlaps and without them, respectively. The error budget for Harmony's RSSH estimate sets the upper bound of the phase synchronization error to $0.06°$. Thus, the correction algorithm meets the requirement.

We also run the algorithm with an alternative phase sync residual. We consider Gaussian-shaped PSD, for the stochastic process describing the phase sync residual. The motivation behind this alternative definition of the synchronization residual's PSD is to assess the performance of the algorithm in the presence of higher-frequency components in the residual. The estimation error for this case is shown in Figure 17. The RMSE increases, compared to the case with the flat PSD, to $0.24°$, and the RMSE after removing the mean of the residual is $0.025°$.

We attribute the larger error to the presence of higher-frequency components in the residual. The presence of higher-frequency components means that the residual, which is the signal to be estimated, changes more rapidly with time. The algorithm estimates the residual by integrating the finite difference of the residual. As the derivative of the residual increases, there is a larger part of the residual that changes within the sampling period of the finite differences. Thus, the estimation error increases. Regardless of the larger estimation error, the algorithm reduces the phase error by at least an order of magnitude for both forms of the phase sync residual.

We now return to the results pertaining to the residual with the flat PSD. Figure 10 shows the estimate error in terms of height. The image is the difference between the RSSH corrected with overlaps of Figure 8, and the RSSH of the scene 7. The RSSH of the scene is mapped into subswaths to account for the TOPSAR operation before computing the difference. It is noteworthy that the error is reduced to the order of $1\,\mathrm{cm}$, while the synchronization residual before correction fluctuates from approximately $-1.5\,\mathrm{m}$ to $1.5\,\mathrm{m}$.

We highlight to the reader that the corrected heights in Figure 8 are fictitious and not a realistic representation of the corrected RSSH product. They are fictitious because they do not include any errors, random or systematic, other than the residual from the phase synchronization error that the correction fails to remove. Such a result would never be visible in the real data, as it would be impossible to remove the measurement noise. However, we are choosing to show the results in this manner to highlight the effect of the correction without any other factors affecting the visualization of the results. Furthermore, we note to the reader that while the measurement noise is removed from the data for the purposes of visualization, the correction is run with noisy observations in accordance with the phase model of (11) and the statistics defined in (21).

In addition to the estimate error shown in Figure 9, and the RMSE which provide global metrics of the algorithm's performance, we use the semivariograms of the signal prior to, and post correction to study the algorithm in terms of spatial lag. Before discussing the features of the directional semivariograms in Figures 11 and 12, we note that since the synchronization residual dominates the retrieved signal prior to correction, the semivariograms describe the statistical properties of the residual. We have verified this finding by computing the directional semivariograms of the synchronization residual and confirming that they closely match those of the uncorrected noisy signal.

The directional semivariograms in Figures 11 and 12 show that the principal direction of continuity of the uncorrected signal is ground range. We can readily confirm this by looking at the retrieved RSSH prior to correction in the bottom panel of Figure 7, where we see the synchronization residual producing horizontal stripes within each subswath. The range of spatial correlation is $117\,\mathrm{km}$ in the ground range direction, and $7.5\,\mathrm{km}$ in the azimuth direction. The strong anisotropy

is because the sync residual is a 1D signal in time that is mapped to two dimensions by the operation of the instrument and formation of the image. Within a burst, the signal varies only with azimuth, or equivalently sensing time. The switching of the instrument between different subswaths introduces a ground range dependence [21] to the synchronization residual, while the cycle time between adjacent bursts introduces discontinuities in azimuth.

In Figure 13 we take the result of correcting the RSSH with the overlap regions, and we add the measurement noise back, as predicted by the XTI model. We then filter the result to a $5\,\mathrm{km} \times 5\,\mathrm{km}$ resolution to reduce the noise, at the cost of reducing the resolution by a factor of 5 in each dimension. It is striking that the pre-correction synchronization-error-dominated signal becomes a noise-limited signal post-correction. In terms of correction, this is a positive result as it shows that retrieving the geospatial signal is possible, despite the synchronization residual dominating the error budget of the signal. Finally, the result reveals that the RSSH of this scene lies at the edge of the interferometric performance of the instrument—$8\,\mathrm{cm}$ at $5\,\mathrm{m\,s^{-1}}$ wind speeds at a resolution of $3\,\mathrm{km} \times 3\,\mathrm{km}$ [8]—in line with our expectations.

Figures 14 and 15 show that the spatial dependence of the corrected RSSH are significantly different from those before the correction. The variance in both directions shows an order of magnitude decrease. The ground-range semivariogram shows spatial independence, consistent with the white noise that dominated the corrected RSSH prior to filtering, up to lags of $60\,\mathrm{km}$ and an upwards trend for larger lags. The trend is likely due to the increasing variance of the measurement error at the mid- to far range. The azimuth semivariogram shows spatial independence for all lags. We postulate that this is because the noise dominates the signal, making the geophysical signature not visible, and because the dependence of the noise's variance on azimuth is weak. Importantly, the signature of the synchronization residual is missing in both directions at all lags.

C. Correction Errors and Algorithm Limitations

During our simulations of the sensing timeline and the correction algorithm, we have arrived to the conclusion that there are three effects that can cause errors in the correction. The first effect is due to the incorrect azimuth positioning of scatterers caused by their radial motion [40]. If the translation of scatterers in the averaged spectral diversity phase is the same as the translation in the interferogram, then the estimated phase that will be applied to the interferogram to correct the synchronization residual will also have the same translation, and the correction will not be affected. In cases, however, where the motion of the scatterers leads to different translations in each subaperture, the spectral diversity phases will be offset relative to one another. The sensing time assigned to each subaperture will be wrong by different amounts, leading to incoherent averaging and estimation errors.

We recommend two potential solutions to this error. The first solution is to form the subapertures from the raw data, then focus to obtain subaperture SAR images, rather than running the algorithm on subapertures formed from the focused SAR images. Thus, each subaperture will have the correct sensing time, and resampling and averaging can be done without errors. The second solution is to use the Doppler centroid of the subapertures, retrieved either through Doppler centroid anomaly or through ATI [41], [42], to estimate the velocity and the azimuth translation due to the radial motion of the scatterers. We can then use the estimate to correct for the misregistration, prior to correcting.

The second error comes from insufficient sampling of the synchronization residual's derivative. The insufficient sampling occurs when the subaperture duration is not an integral multiple of the sampling period in azimuth. This condition can be readily derived from (5). For the sampling of the derivative to have no gaps, the kth sample of subaperture $i+1$ must coincide in time with the $(k+n)$th sample of the ith subaperture. Setting $t_{c,i}[k+n]$ equal to $t_{c,i+1}[k]$ and solving for the sampling period gives

$$T = \frac{T_a}{nN}, \tag{26}$$

where T_a/N is the subaperture integration time, and n is the offset in samples before the sensing times coincide.

In cases where (26) does not hold, the interval over which the algorithm computes the finite phase difference is smaller than the step between consecutive samples of the derivative. This leads to gaps in the sampling of the derivative, which cause estimation errors. As the estimator performs an integration step, these errors accumulate. Our simulations confirm that the estimation errors scale with the variance of the synchronization residual. Thus, it is beneficial to match the subaperture integration time to, or a multiple of, the sampling period of the derivative. Practically, this is difficult to achieve because of the bursts produced by TOPSAR, and because of the antenna weighting which would tend to weigh subaperture samples differently, changing the effective sensing times.

A third potential source of error is the sea-state bias. Sea-state bias in altimetric measurements of the ocean surface refers to an error in the measurement that depends on the degree of turbulence of the scene [43]. The analysis in [8], shows that the sea-state bias in Harmony's RSSH measurement depends on the surface elevation variance spectrum, and the modulation of the backscattering by the surface. The variation of the surface elevation variance spectrum within the aperture time is relatively small. Thus, the look dependence of the bias is not significant. Furthermore, Harmony will measure the surface elevation variance spectrum; based on this measurement, we plan to estimate the sea-state bias and remove it from the interferogram. Therefore, only a residual will remain.

Finally, as shown in section V-B and discussed in section VI-B, a limitation of the algorithm is the inability to estimate the mean value of the synchronization residual. In essence, the estimator integrates the finite differences to obtain the signal but has no way of solving for the integration constant. In (15), we postulate that the mean value of the signal is $0°$. Therefore, the estimator centers the solution about $0°$ which leads to a bias in the solution equal to the mean value of ψ_c. The consequence is that if the mean value of ψ_c is large

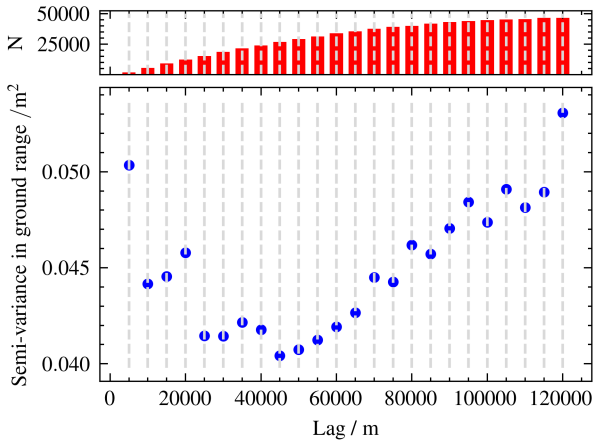

Fig. 14. The directional semivariogram of the corrected RSSH in the ground range direction. The semivariogram shows spatial independence.

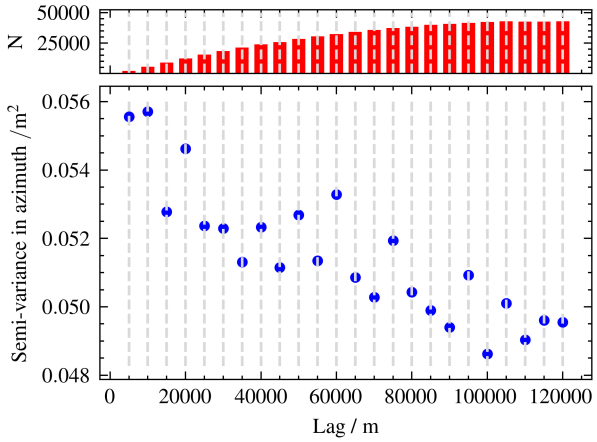

Fig. 15. The directional semivariogram of the corrected RSSH in the azimuth range direction. The semivariogram shows spatial independence.

enough to cause phase wrapping, it will form fringe patterns in the interferogram. In principle, MuSO cannot estimate this unknown constant from the data. A simple solution is to use an external digital elevation model and compare it to the synchronized interferogram to detect the error due to the unknown mean phase.

VII. Conclusion

We have presented an algorithm to remove the phase-synchronization residual that remains in the bistatic SAR signal of Harmony after the GNSS-based synchronization. The algorithm takes advantage of the periodic sampling overlaps between adjacent bursts in azimuth that occur in TOPSAR to improve the long-term sampling of the residual's derivative. Furthermore, our phase model accounts for the interferometric phase due to the motion of the surface, and we have shown that with a system like Harmony that can produce SAR images from individual phase centers this component of the phase can be estimated and removed.

To assess the validity of the correction, we have developed a simulation chain that produces acquisitions of the interferometric phase and estimated RSSH from geophysical model outputs describing the scene. The model outputs include wind, currents, directional wave spectra and RSSH. The simulation chain also models realizations of the phase synchronization error according to the power spectral density of the residual. Running the correction on the simulated acquisitions shows that we can remove the effect of the synchronization residual and estimate the RSSH. The correction achieves a root-mean-square error of $0.046°$, which satisfies the limit for the phase synchronization error needed for Harmony to retrieve submesoscale RSSH.

In the future, we plan to improve on the correction algorithm by incorporating the autocorrelation length of the derivative in the estimator. We can derive the autocorrelation length from the PSD of the phase synchronization residual. The autocorrelation of the derivative can then be incorporated in the estimator by using a Wiener filter to reduce the noise in the subaperture phase before running the correction.

Additionally, we have discussed three sources of error in the correction. The first error results from the motion of the surface. Since the instrument will be sampling the ocean surface, the surface will have a mean motion. Thus, the radial component of the motion will cause an azimuth misregistration. If the misregistration varies with subaperture, then the sensing times assigned to the spectral diversity derivatives will be wrong, which will lead to an error. Forming the subapertures directly from the raw data, instead of filtering the focused full aperture data, mitigates this problem. We plan to verify this approach using the Harmony end-to-end simulator. The second error is due to gaps in the sampling of the derivative. The gaps are avoided when the subaperture integration time is an integral multiple of the derivative's sampling period. The final error is the sea-state bias, for which we propose a potential correction based on the estimation of the surface elevation variance spectrum.

Acknowledgment

The authors would like to thank Dr.-Ing. Pau Prats-Iraola and Dr.-Ing. Marc Rodriguez-Cassola for the constructive discussions on the topic.

Appendix
Performance with Gaussian Phase Residual PSD

In an effort of bounding the performance of the data-driven correction, we consider an alternative PSD of the phase residual. We model the phase residual after the GNSS-based synchronization as a stochastic process, $\{\psi_c(t), t \geq 0\}$, as in Section II-B. However, instead of assuming a flat non-zero PSD, we use PSD with a Gaussian shape

$$S_{\psi_c}(f) = \frac{\sigma^2_{\psi_c}}{\sqrt{a\pi}} \mathrm{e}^{-f^2/a}, \tag{27}$$

where

$$a = \frac{{f_{3dB}}^2}{\ln 2}, \tag{28}$$

determines the $3\,\mathrm{dB}$ point, represented by f_{3dB}, of the PSD. Equation (27) has been defined so that its integral over all

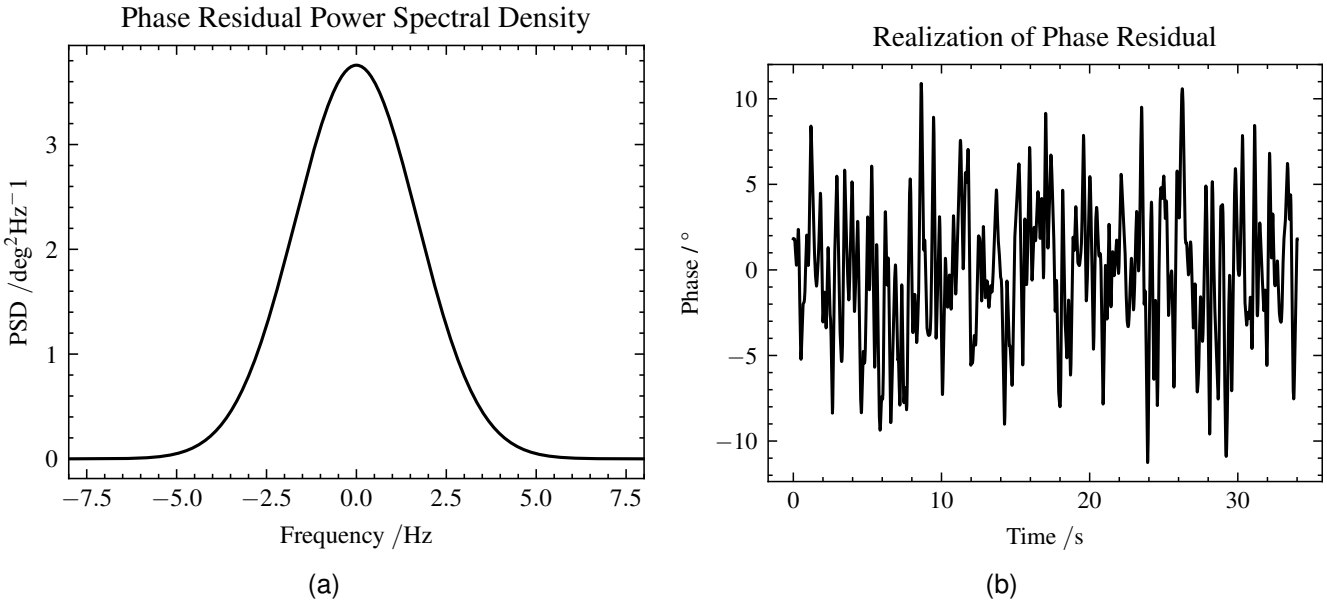

Fig. 16. Alternative phase residual after applying the GNSS-based synchronization scheme has a Gaussian-shaped PSD. (a) The power spectral density. (b) A realization of the stochastic process.

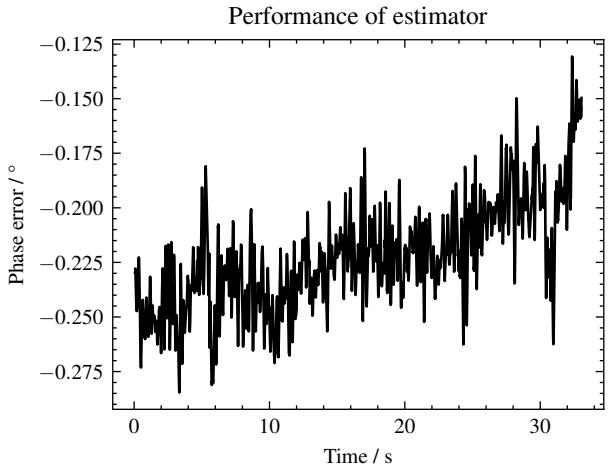

Fig. 17. Estimate error between the true phase synchronization residual and the estimated synchronization residual for a realization of the phase residual with the Gaussian-shaped PSD.

frequencies is the variance of the signal, $\sigma^2_{\psi_c}$, in the same way as the flat spectrum of (1).

We set $\sigma_{\psi_c} = 4°$, and $f_{3dB} = 2\,\mathrm{Hz}$, as in Section II-B. Figure 16a shows the PSD described by (27), with the aforementioned parameters, and Figure 16b illustrates a realization of this signal. Once the phase residual with the alternative PSD has been generated, we proceed with the simulation as explained in Sections III–V-A, keeping all other parameters the same.

We illustrate the error of the estimator in Figure 17. The error is larger than in the case with the flat PSD. We attribute the larger error to the presence of higher frequency components. The RMSE of the estimator is $0.24°$, and the RMSE after removing the mean of the residual is $0.025°$.

REFERENCES

[1] J. C. McWilliams, "Submesoscale currents in the ocean," *Proceedings of the Royal Society A: Mathematical, Physical and Engineering Sciences*, vol. 472, no. 2189, p. 20160117, May 2016.

[2] X. Capet, J. C. McWilliams, M. J. Molemaker, and A. F. Shchepetkin, "Mesoscale to Submesoscale Transition in the California Current System. Part I: Flow Structure, Eddy Flux, and Observational Tests," *Journal of Physical Oceanography*, vol. 38, no. 1, pp. 29–43, Jan. 2008.

[3] A. Mahadevan and A. Tandon, "An analysis of mechanisms for submesoscale vertical motion at ocean fronts," *Ocean Modelling*, vol. 14, no. 3, pp. 241–256, Jan. 2006.

[4] G. Lapeyre and P. Klein, "Impact of the small-scale elongated filaments on the oceanic vertical pump," *Journal of Marine Research*, vol. 64, no. 6, pp. 835–851, Nov. 2006.

[5] L.-L. Fu and R. Ferrari, "Observing Oceanic Submesoscale Processes From Space," *Eos, Transactions American Geophysical Union*, vol. 89, no. 48, pp. 488–488, 2008.

[6] M. Durand, L.-L. Fu, D. P. Lettenmaier, D. E. Alsdorf, E. Rodriguez, and D. Esteban-Fernandez, "The Surface Water and Ocean Topography Mission: Observing Terrestrial Surface Water and Oceanic Submesoscale Eddies," *Proceedings of the IEEE*, vol. 98, no. 5, pp. 766–779, May 2010.

[7] P. López-Dekker, H. Rott, P. Prats-Iraola, B. Chapron, K. Scipal, and E. D. Witte, "Harmony: An Earth Explorer 10 Mission Candidate to Observe Land, Ice, and Ocean Surface Dynamics," in *IGARSS 2019 - 2019 IEEE International Geoscience and Remote Sensing Symposium*, Jul. 2019, pp. 8381–8384.

[8] A. Theodosiou, M. Kleinherenbrink, and P. López-Dekker, "Wide-Swath Ocean Altimetry Using Multisatellite Single-Pass Interferometry," *IEEE Transactions on Geoscience and Remote Sensing*, vol. 61, pp. 1–21, 2023.

[9] G. Krieger, A. Moreira, H. Fiedler, I. Hajnsek, M. Werner, M. Younis, and M. Zink, "TanDEM-X: A Satellite Formation for High-Resolution SAR Interferometry," *IEEE Transactions on Geoscience and Remote Sensing*, vol. 45, no. 11, pp. 3317–3341, Nov. 2007.

[10] M. Younis, R. Metzig, and G. Krieger, "Performance prediction of a phase synchronization link for bistatic SAR," *IEEE Geoscience and Remote Sensing Letters*, vol. 3, no. 3, pp. 429–433, Jul. 2006.

[11] N. J. Willis, *Bistatic Radar*. Institution of Engineering and Technology, Jan. 2004.

[12] J. L. Auterman, "Phase stability requirements for bistatic SAR," in *IEEE Nat. Radar Conf., Atlanta, 1984*, 1984, pp. 45–52.

[13] D. Massonnet and H. Vadon, "EES-1 internal clock drift measured by interferometry," *IEEE Transactions on Geoscience and Remote Sensing*, vol. 33, no. 2, pp. 401–408, Mar. 1995.

[14] H. Cantalloube, M. Wendler, V. Giroux, P. Dubois-Fernandez, and G. Krieger, "Challenges in SAR processing for airborne bistatic acquisitions," in *Proceedings EUSAR 2004*, VDE, Ed., vol. 2. Ulm, Germany: VDE Verlag, 2004, pp. 577–580.

[15] M. Rodriguez-Cassola, P. Prats, D. Schulze, N. Tous-Ramon, U. Steinbrecher, L. Marotti, M. Nannini, M. Younis, P. Lopez-Dekker, M. Zink, A. Reigber, G. Krieger, and A. Moreira, "First Bistatic Spaceborne SAR Experiments With TanDEM-X," *IEEE Geoscience and Remote Sensing Letters*, vol. 9, no. 1, pp. 33–37, Jan. 2012.

[16] E. Rodrigues-Silva, M. Rodriguez-Cassola, G. Krieger, and A. Moreira, "GNSS-Based Phase Synchronization for Bistatic and Multistatic Synthetic Aperture Radar," *IEEE Transactions on Geoscience and Remote Sensing*, vol. 62, pp. 1–14, 2024.

[17] A. Theodosiou and P. López-Dekker, "On the Sensitivity to Height and Motion of Bistatic SAR Interferometry: A Spectral View," *IEEE Transactions on Geoscience and Remote Sensing*, vol. 62, pp. 1–12, 2024.

[18] A. Reigber, P. Prats, and J. Mallorqui, "Refined estimation of time-varying baseline errors in airborne SAR interferometry," *IEEE Geoscience and Remote Sensing Letters*, vol. 3, no. 1, pp. 145–149, Jan. 2006.

[19] P. Prats, R. Scheiber, A. Reigber, C. Andres, and R. Horn, "Estimation of the Surface Velocity Field of the Aletsch Glacier Using Multibaseline Airborne SAR Interferometry," *IEEE Transactions on Geoscience and Remote Sensing*, vol. 47, no. 2, pp. 419–430, Feb. 2009.

[20] M. Azcueta and S. Tebaldini, "Non-Cooperative Bistatic SAR Clock Drift Compensation for Tomographic Acquisitions," *Remote Sensing*, vol. 9, no. 11, p. 1087, Nov. 2017.

[21] F. De Zan and A. Monti Guarnieri, "TOPSAR: Terrain Observation by Progressive Scans," *IEEE Transactions on Geoscience and Remote Sensing*, vol. 44, no. 9, pp. 2352–2360, Sep. 2006.

[22] D. Liang, H. Zhang, K. Liu, D. Liu, and R. Wang, "Phase Synchronization Techniques for Bistatic and Multistatic Synthetic Aperture Radar: Accounting for frequency offset," *IEEE Geoscience and Remote Sensing Magazine*, vol. 10, no. 3, pp. 153–167, Sep. 2022.

[23] M. D'Errico, *Distributed Space Missions for Earth System Monitoring*. Springer Science & Business Media, 2012, vol. 31.

[24] A. J. Owens, "An algorithm for generating fluctuations having any arbitrary power spectrum," *Journal of Geophysical Research: Space Physics*, vol. 83, no. A4, pp. 1673–1675, 1978.

[25] P. Prats and J. Mallorqui, "Estimation of azimuth phase undulations with multisquint processing in airborne interferometric SAR images," *IEEE Transactions on Geoscience and Remote Sensing*, vol. 41, no. 6, pp. 1530–1533, Jun. 2003.

[26] K. Ouchi, "On the multilook images of moving targets by synthetic aperture radars," *IEEE Transactions on Antennas and Propagation*, vol. 33, no. 8, pp. 823–827, Aug. 1985.

[27] R. M. Goldstein and H. A. Zebker, "Interferometric radar measurement of ocean surface currents," *Nature*, vol. 328, no. 6132, pp. 707–709, Aug. 1987.

[28] I. G. Cumming and F. H.-c. Wong, *Digital Processing of Synthetic Aperture Radar Data: Algorithms and Implementation*, ser. Artech House Remote Sensing Library. Boston: Artech House, 2005.

[29] N. B. D. Bechor and H. A. Zebker, "Measuring two-dimensional movements using a single InSAR pair," *Geophysical Research Letters*, vol. 33, no. 16, 2006.

[30] M. Seymour and I. Cumming, "Maximum likelihood estimation for SAR interferometry," in *Proceedings of IGARSS '94 - 1994 IEEE International Geoscience and Remote Sensing Symposium*, vol. 4, Aug. 1994, pp. 2272–2275 vol.4.

[31] N. Cressie, "Fitting variogram models by weighted least squares," *Journal of the International Association for Mathematical Geology*, vol. 17, no. 5, pp. 563–586, Jul. 1985.

[32] ——, *Statistics for Spatial Data*. John Wiley & Sons, Mar. 2015.

[33] O. Schabenberger and C. A. Gotway, *Statistical Methods for Spatial Data Analysis*. New York: Chapman and Hall/CRC, Feb. 2017.

[34] Ifremer, University of Brest, CNRS, IRD, Laboratoire d'Océanographie Physique et Spatiale (LOPS), IUEM, Brest, France, "Data from MARS2D model simulations, "Modelling and Analysis for Coastal Research" (MARC) project."

[35] ——, "Data from MARS3D model simulations, "Modelling and Analysis for Coastal Research" (MARC) project."

[36] ——, "Data from WaveWatch III model simulations, "Modelling and Analysis for Coastal Research" (MARC) project."

[37] L. Pineau-Guillou, "PREVIMER. Validation des modèles hydrodynamiques 2D des côtes de la Manche et de l'Atlantique," Jun. 2013.

[38] P. Lazure and F. Dumas, "An external–internal mode coupling for a 3D hydrodynamical model for applications at regional scale (MARS)," *Advances in Water Resources*, vol. 31, no. 2, pp. 233–250, Feb. 2008.

[39] WW3DG, "User manual and system documentation of WAVEWATCH III version 6.07, the WAVEWATCH III development group," *Tech. Note 326 pp. + Appendices, NOAA/NWS/NCEP/MMAB*, 2019.

[40] R. K. Raney, "Synthetic Aperture Imaging Radar and Moving Targets," *IEEE Transactions on Aerospace and Electronic Systems*, vol. AES-7, no. 3, pp. 499–505, May 1971.

[41] D.-j. Kim, W. Moon, D. Moller, and D. Imel, "Measurements of ocean surface waves and currents using L- and C-band along-track interferometric SAR," *IEEE Transactions on Geoscience and Remote Sensing*, vol. 41, no. 12, pp. 2821–2832, Dec. 2003.

[42] H. C. Graber, D. R. Thompson, and R. E. Carande, "Ocean surface features and currents measured with synthetic aperture radar interferometry and HF radar," *Journal of Geophysical Research: Oceans*, vol. 101, no. C11, pp. 25 813–25 832, 1996.

[43] D. Vandemark, B. Chapron, J. Sun, G. H. Crescenti, and H. C. Graber, "Ocean Wave Slope Observations Using Radar Backscatter and Laser Altimeters," *Journal of Physical Oceanography*, vol. 34, no. 12, pp. 2825–2842, Dec. 2004.

Andreas Theodosiou was born in Nicosia, Cyprus, in 1993. He received the B.A. and M.Eng. degrees in electrical and information sciences from the University of Cambridge, Cambridge, UK, in 2018. He received the Ph.D. degree in wide-swath ocean altimetry with bistatic synthetic-aperture radar (SAR) interferometry from the Delft University of Technology, Delft, The Netherlands, in 2025.

From 2018 to 2019, he was with the RF Payloads Section, European Space Agency, Noordwijk, The Netherlands. In 2019, he joined the Faculty of Civil Engineering and Geoscience, Delft University of Technology, Delft, The Netherlands, to work on performance modeling, simulation, and retrieval algorithms for Earth Explorer 10 mission, Harmony. In 2024, he joined the European Space Agency, Noordwijk, The Netherlands as a mission performance engineer. His research interests include future SAR mission concepts and ocean remote sensing.

Paco López-Dekker (Senior Member, IEEE) was born in Nijmegen, The Netherlands, in 1972. He received the Ingeniero degree in telecommunication engineering from the Universitat Politècnica de Catalunya (UPC), Barcelona, Spain, in 1997, the M.S. degree in electrical and computer engineering from the University of California at Irvine, Irvine, CA, USA, in 1998, under the Balsells Fellowship, and the Ph.D. degree in clear-air imaging radar systems to study the atmospheric boundary layer from the University of Massachusetts, Amherst, MA, USA, in 2003.

In 2003, he joined Starlab Barcelona, Barcelona, where he worked on the development of Global Navigation Satellite Systems Reflectometry (GNSS-R) sensors and techniques. From 2004 to 2006, he was a Visiting Professor with the Department of Telecommunications and Systems Engineering, Universitat Autònoma de Barcelona, Bellaterra, Spain. In March 2006, he was awarded a Ramon y Cajal Grant to conduct pioneering research on bistatic synthetic aperture radar (SAR) at the Remote Sensing Laboratory, UPC. From November 2009 to August 2016, he led the SAR Missions Group, Microwaves and Radar Institute, German Aerospace Center, Weßling, Germany. In 2016, he joined the Geoscience and Remote Sensing Department, Faculty of Civil Engineering and Geosciences, Delft University of Technology, Delft, The Netherlands, as an Associate Professor, and has held the position of Professor since 2025. He has been deeply involved in the development of several radar missions and mission proposals and is the Lead Investigator of the Harmony European Space Agency (ESA) Earth Explorer 10 Mission. He has coauthored over 50 peer-reviewed journal articles and more than 125 conference contributions in a broad range of topics related to radar remote sensing.